



Revealing Driving Forces in Quantum Dot Supercrystal Assembly

Marino, E., Kodger, T. E., Wegdam, G. H., & Schall, P.

This article is made publically available in the institutional repository of Wageningen University and Research, under article 25fa of the Dutch Copyright Act, also known as the Amendment Taverne.

Article 25fa states that the author of a short scientific work funded either wholly or partially by Dutch public funds is entitled to make that work publicly available for no consideration following a reasonable period of time after the work was first published, provided that clear reference is made to the source of the first publication of the work.

For questions regarding the public availability of this article, please contact openscience.library@wur.nl.

Please cite this publication as follows:

Marino, E., Kodger, T. E., Wegdam, G. H., & Schall, P. (2018). Revealing Driving Forces in Quantum Dot Supercrystal Assembly. *Advanced Materials*, 30(43), [1803433]. <https://doi.org/10.1002/adma.201803433>

Revealing Driving Forces in Quantum Dot Supercrystal Assembly

Emanuele Marino, Thomas E. Kodger, Gerard H. Wegdam, and Peter Schall*

The assembly of semiconductor nanoparticles, quantum dots (QDs), into dense crystalline nanostructures holds great promise for future optoelectronic devices. However, knowledge of the sub-nanometer scale driving forces underlying the kinetic processes of nucleation, growth, and final densification during QD assembly remains poor. Emulsion-templated assembly has recently been shown to provide good control over the bulk condensation of QDs into highly ordered 3D supercrystals. Here, emulsion-templated assembly is combined with in situ small-angle X-ray scattering to obtain direct insight into the nanoscale interactions underlying the nucleation, growth, and densification of QD supercrystals. At the point of supercrystal nucleation, nanoparticles undergo a hard-sphere-like crystallization into a hexagonal-close-packed lattice, slowly transforming into a face-centered-cubic lattice. The ligands play a crucial role in balancing steric repulsion against attractive van der Waals forces to mediate the initial equilibrium assembly, but cause the QDs to be progressively destabilized upon densification. The rich detail of this kinetic study elucidates the assembly and thermodynamic properties that define QD supercrystal fabrication approaching single-crystal quality, paving the way toward their use in optoelectronic devices.

Colloidal semiconductor nanocrystals or quantum dots (QDs) represent an important class of materials that has drawn considerable attention in the last few years. The possibility of bandgap tuning by varying dot size is attractive for both lighting and energy industry, enabling applications such as full-color screens and light emitting diodes,^[1] photodetectors,^[2] solar cells,^[3] and lasers.^[4] Most applications require the assembly of QDs into thin films at the highest possible packing fraction. In lasing, the threshold for stimulated emission depends linearly on the volume fraction of QDs^[5]; in electronics, 3D charge percolation is only possible when the volume fraction is higher than 15%.^[6] While many different QD superstructures have

been assembled, spanning the parameter space in compositional and structural complexity,^[7] the nanoscale interactions directing the assembly process remain poorly understood. Importantly, the ligands are believed to play a crucial role in the assembly process,^[8] yet their function in mediating QD interactions during kinetic assembly and final aggregation remains unclear.

Recently, an emulsion droplet-templated assembly method was developed to produce high-volume fraction nanoparticle superstructures.^[9] The method relies on the evaporation of a volatile hydrophobic solvent from an oil-in-water emulsion where each oil droplet contains a dispersion of nanoparticles, and allows excellent control over slow drying rates. After complete evaporation, the final product consists of spherical colloidal superstructures composed of visually ordered nanoparticles or supercrystals. The approach is applicable to nearly any kind of nanoparticle, both hydrophobic


and hydrophilic, by using, respectively, oil-in-water or water-in-oil emulsions. The controlled slow evaporation sets the rate of change of volume fraction of the QD dispersions, enabling direct control over the crystallization process, which ultimately determines the crystal quality. Consequently, this technique is uniquely suited to achieve high-quality superstructures and study the driving forces of their assembly in detail, unlike other drying techniques such as drop casting or spin coating that are less controlled and convenient to study.

Understanding the driving forces in QD crystallization is paramount to maximizing order in superstructures, which is the first step toward unraveling novel physical properties, such as minibands,^[10] that will ultimately set the performance limits of QD devices.

In this work, we use in situ synchrotron X-ray scattering to obtain direct insight into the formation of QD supercrystals and elucidate the underlying particle interactions during assembly. We implement a new method to collect small angle X-ray scattering (SAXS) patterns in real time during evaporation of QD-containing emulsion droplets and follow the nucleation, growth, and crystal densification process. By imposing a limit on the rate of evaporation, we are able to follow key moments of the QD assembly in great detail. We find that QD supercrystals nucleate into a hexagonal-close-packed (HCP) lattice, which slowly transforms into a face-centered-cubic (FCC) lattice and

E. Marino, Dr. T. E. Kodger, Prof. G. H. Wegdam, Prof. P. Schall
Van der Waals–Zeeman Institute
University of Amsterdam
Science Park 904, 1098XH Amsterdam, The Netherlands
E-mail: p.schall@uva.nl

Dr. T. E. Kodger
Physical Chemistry and Soft Matter
Wageningen University and Research
Stippeneng 4, 6708WE, Wageningen, The Netherlands

 The ORCID identification number(s) for the author(s) of this article can be found under <https://doi.org/10.1002/adma.201803433>.

DOI: 10.1002/adma.201803433

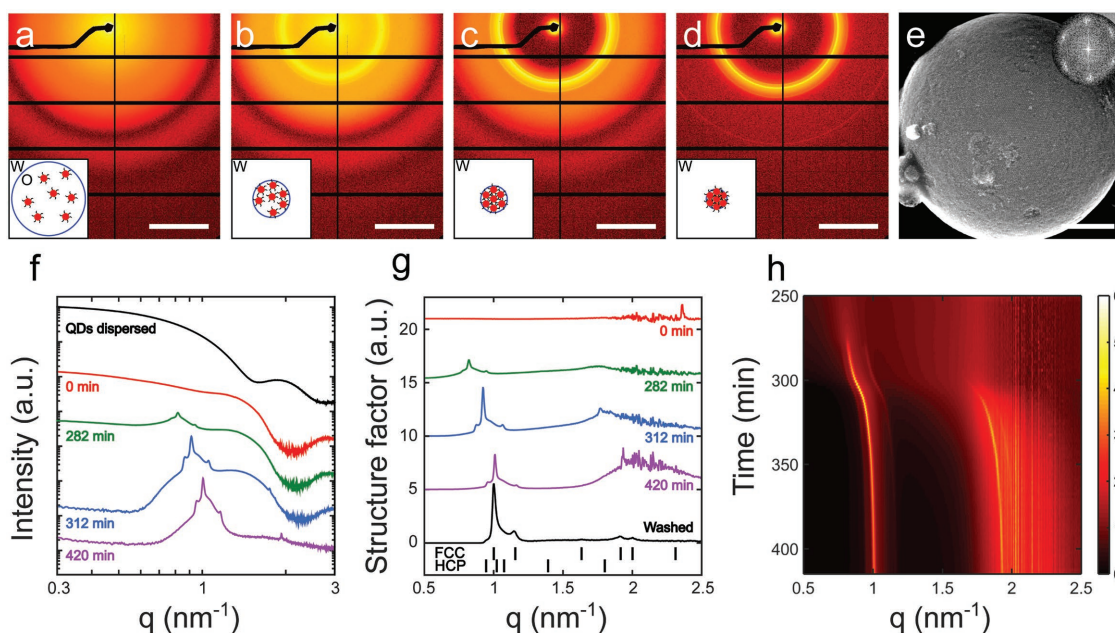


Figure 1. In situ observation of QD supercrystal assembly. a–d) 2D SAXS patterns obtained from crystallizing CdSe QDs confined in oil droplets of an oil-in-water emulsion. Patterns are recorded during drying of the oil droplets, at (a) 0 min, (b) 282 min, (c) 312 min, and (d) 420 min. Scale bars indicate 1 nm^{-1} . Insets show sketches of the drying oil droplets containing the QDs. e) Scanning electron microscope image of an 800 nm spherical supercrystal showing highly ordered 5.4 nm QDs. Scale bar indicates 200 nm. Inset: fast Fourier transform of the SEM image displaying sixfold symmetry. f) Azimuthally averaged scattering profiles $I(q)$ of dilute QDs dispersed in hexane (upper black curve), and QDs during crystallization in the drying oil-in-water emulsion (colored curves). Intensity profiles have been shifted for clarity. g) Effective structure factor $S_{\text{eff}}(q)$ of the crystallizing QDs extracted from the intensity $I(q)$ in (f) (colored curves), and structure factor of the final dried supercrystals, re-dispersed in water with surfactant (black curve). Starting from $S_{\text{eff}}(q) = 1$, typical for noninteracting particles, the structure factor develops peaks characteristic of FCC and HCP crystal order. Ticks at the bottom demarcate the expected positions of FCC and HCP diffraction peaks for the final dried supercrystals. h) Contour plot showing the full time evolution of the effective structure factor $S_{\text{eff}}(q,t)$ during the self-assembly process. Color bar on the right indicates the magnitude of $S(q)$.

densifies. While nucleation and early growth are consistent with effective hard-sphere behavior of ligand-stabilized QDs, a balance of sterically repulsive ligands and attractive van der Waals interactions dictates the later stages of assembly until permanent aggregation of the supercrystals. These results demonstrate the important interplay of entropic nucleation and nanoscale interactions in the drying-induced assembly of nanostructures.

Hydrophobic cadmium selenide (CdSe), QDs are synthesized following a reported procedure (see Supporting Information).^[11] Oleate ligands grafted on the QD surface provide colloidal stability for several years in apolar solvents by steric repulsion and are well suited as colloidal building blocks for close-packed superstructures.^[12] X-ray scattering from a dilute dispersion of the synthesized CdSe QDs in hexane yields a form factor consistent with spheres of diameter $\sigma_{\text{QD}} = 5.4 \text{ nm}$, and a polydispersity of 7% (Figure S1, Supporting Information). Adding this dilute QD dispersion to an aqueous solution of surfactant, we obtain a two-phase system that is emulsified by vortexing the container, leading to polydisperse droplets of QD dispersion suspended in water, stabilized by the surfactant (Figure S2, Supporting Information). Upon evaporation of the hexane droplets, the volume fraction, ϕ , of the QDs increases, eventually forcing the system from a dilute colloidal gas phase with negligible particle–particle interactions to a dense solid phase with interacting particles. The rate of evaporation sets the rate of change of volume fraction in time, $d\phi/dt$; this quantity

represents the colloidal equivalent the colloidal equivalent to the rate of temperature quench in atomic systems, which plays a crucial role in the crystallization and final quality of atomic crystals. The evaporation rate is ultimately defined by the temperature and solubility of the apolar solvent in the aqueous phase.^[13] To control the evaporation rate while simultaneously measuring SAXS, we developed a setup in which the emulsion is continuously allowed to flow through a $10 \mu\text{m}$ walled quartz capillary while evaporating from a thermo-stated reservoir (Figure S3, Supporting Information). 2D scattering patterns recorded at a rate of 0.6 min^{-1} reveal the kinetic details of the QD crystallization process.

Scattering patterns show the evolution of the QD superstructure in Figure 1. Initially, we observe a diffuse pattern (Figure 1a), which after a few minutes of drying at $40 \text{ }^\circ\text{C}$ develops a broad ring (Figure 1b), followed by the sudden occurrence of narrower and more pronounced rings (Figure 1c), which sharpen as they expand outward and the diffuse background vanishes (Figure 1d). The initial diffuse pattern reflects the form factors of both the micrometer-sized emulsion droplets and the dilute dispersion of nanometer-sized QDs. Subsequently, the appearance of a broad ring indicates the emergence of short-range order within the concentrated QD dispersion. The sudden occurrence of narrower and more pronounced rings reveals the formation of crystals within the dense QD dispersions (Figure 1c); their azimuthal symmetry indicates the presence of many supercrystals within the scattering volume, whose superposition results

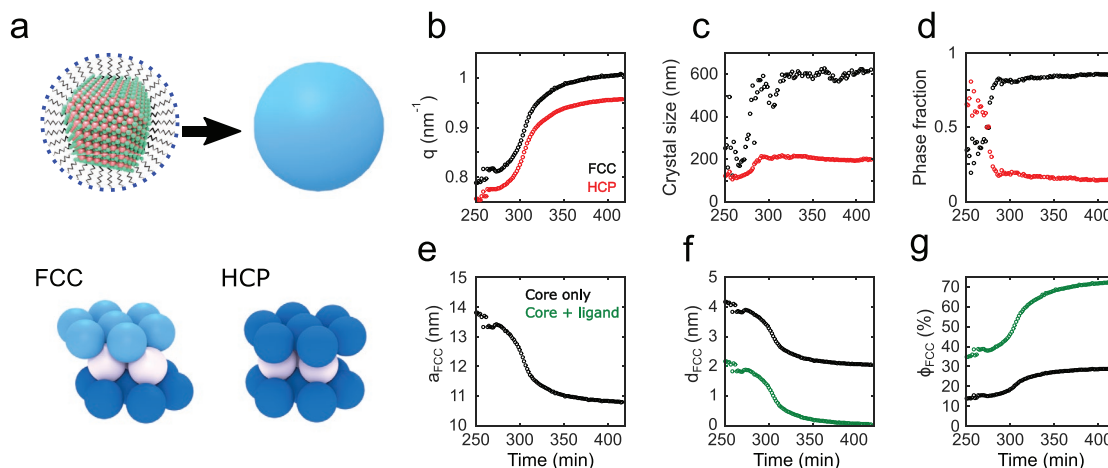


Figure 2. Supercrystal size, lattice parameter and phase fraction. a, top) Schematic relating the CdSe QDs (Cd atoms in red, Se in green) with ligands to effective hard spheres. The assembly kinetics can be described in terms of hard-sphere behavior when including the effective ligand length $l = 1$ nm. (a, bottom) Schematic showing FCC and HCP hard-sphere packing. b) Peak position $q(t)$ followed in time for FCC (111) and HCP (100) peaks. c) Average crystal domain size ξ estimated with the Scherrer formula $\xi(t) \approx 2\pi K / \Delta q(t)$, where $K = 1$ for a spherical crystal and $\Delta q(t)$ is the full-width-half-maximum of FCC (111) and HCP (100) peaks. d) Phase fraction f_{FCC} and f_{HCP} of FCC and HCP crystals calculated as $f_{\text{FCC,HCP}}(t) = A_{\text{FCC,HCP}}(t) / [A_{\text{FCC}}(t) + A_{\text{HCP}}(t)]$, where $A_{\text{FCC,HCP}}(t) = I_{\text{FCC,HCP}}(t) \times \xi_{\text{FCC,HCP}}(t)$ and $I_{\text{FCC,HCP}}$ is the height of the 111 (100) peak. e–g) Evolution of structural parameters for FCC phase: (e) lattice parameter $a_{\text{FCC}}(t) = 2\pi\sqrt{3} / q_{111}(t)$, (f) QD surface-to-surface distance $d_{\text{FCC}}(t) = [a_{\text{FCC}}(t) / \sqrt{2}] - \sigma_{\text{QD}}$, and (g) volume fraction $\phi_{\text{FCC}}(t) = (2\pi/3) \times [\sigma_{\text{QD}} / a_{\text{FCC}}(t)]^3 \times 100\%$, (black symbols). To include the ligand contribution we substituted σ_{QD} with σ_{eff} (green symbols).

in a powder-like diffraction pattern. Finally, the expansion of the rings and disappearance of the diffuse background indicates a compression of the QD crystal lattice and simultaneous drying and vanishing of the emulsion droplets. Inspecting the final product under the electron microscope reveals spherical supercrystals of diameters between 50 and 1000 nm (Figure S4, Supporting Information), exhibiting clear hexagonal order at the surface, as shown in Figure 1e (a full-scale image is shown in Figure S11, Supporting Information). The sixfold symmetry is confirmed by the fast Fourier transform of the real-space image as shown in the inset of the figure.

To follow the crystallization process in more detail, we plot the azimuthally averaged scattered intensity $I(q, t)$ in Figure 1f and Figure S5 in the Supporting Information. The corresponding structure factor $S(q, t)$ is obtained by dividing $I(q, t)$ by the effective form factor, which arises from the scattering of dispersed QDs within the emulsion droplets, the emulsion droplets themselves, and the surfactant in the aqueous phase. As direct modeling of the evolving form factor is challenging due to droplet polydispersity and size-dependent rates of evaporation, we take $F_{\text{eff}}(q) \equiv I(q, t = 0)$ as effective form factor and calculate $S_{\text{eff}}(q, t) = I(q, t) / F_{\text{eff}}(q)$. This choice is reasonable, since at the beginning of the experiment, the QD dispersion is very dilute ($\phi = 0.09\%$) and therefore $S(q, 0) = 1$. The resulting $S_{\text{eff}}(q, t)$ displays the emergence of reflections as shown in Figure 1g. Reflections emerge at $t = 275$ min, and grow and sharpen in time as shown by the full time evolution of $S_{\text{eff}}(q, t)$ in Figure 1h. The detectable onset of nucleation at $t = 275$ min is clearly shown in the emergence of the first reflection of the structure factor at $q = 0.8 \text{ nm}^{-1}$, while the s-shaped evolution of $S_{\text{eff}}(q, t)$ between 300 and 310 min demarcates the complete phase transition from fluid to crystal, at which the particles densify rapidly and the reflections shift to higher q . Limited by the ability to discern the broad reflections ascribed to small crystallites, crystals can only be detected when they

have reached a large enough size, which occurs at $t \geq 275$ min; however, the actual moment of nucleation takes place slightly earlier, around $t = 250$ min (Figure S5b, Supporting Information). We also show the structure factor of completely dried and re-suspended supercrystals in Figure 1g (bottom), which we extracted using $S(q) = I(q) / F_{\text{QD}}(q)$, where $F_{\text{QD}}(q)$ is the form factor of the fully dispersed QDs in hexane. The positions of reflections show ratios $q_i / q_1 = 1, \sqrt{4/3}, \sqrt{8/3}, \sqrt{11/3}, \sqrt{12/3}$, where q_i is the position of the i th reflection; these ratios are consistent with FCC packing, as shown by comparison with the reference positions of reflections. Interestingly, at early times, additional features reveal the occurrence of a minority crystal phase. These features are consistent with the HCP crystal structure. In fact, FCC and HCP differ from one another merely by the stacking sequence of HCP layers (Figure 2a). As their free energy difference is extremely small, of the order of $10^{-3} \text{ k}_B\text{T}$ favoring FCC,^[14] both lattices often occur together in hard-sphere systems. Therefore, either FCC or HCP could stabilize critical nuclei. From the intensity of the relative contribution of FCC and HCP to the structure factor, we conclude that initially, HCP dominates, while at later stages, supercrystals are primarily FCC with a minority HCP phase.

We further quantify this phase change using the peak widths and heights determined by Gaussian fitting to extract, respectively, mean crystalline domain size, $\xi(t)$, and relative fraction of FCC and HCP crystalline phases. These are shown together with the FCC (111) and HCP (100) peak positions in Figure 2b–d; the s-shaped pattern is clearly reproduced with both crystal phases shifting synchronously toward higher q . Remarkably, within only 30 min, the average crystal size quickly increases to 600 nm for the FCC phase and 200 nm for the HCP phase (Figure 2c), each crystallite containing 10^4 – 10^6 QDs. A comparison with literature values reveals that these crystal sizes are 6–60 times larger than what has been achieved so far for interfacial assembly,^[15] as well as spin coating,^[16] and

are comparable to early reports for complex, ultra-slow self-assembly methods.^[17] The relative fractions, f_{FCC} and f_{HCP} , of FCC and HCP crystalline phases (Figure 2d) show that, indeed, the early stages of assembly are governed by a dominance of HCP, $f_{\text{HCP}} = 0.8$, with sizes of 100 nm, suggesting a critical radius of nucleation of 50 nm. Remarkably, f_{FCC} and f_{HCP} cross over at around 275 min transitioning supercrystals to mostly FCC at the end of the experiment, $f_{\text{FCC}} = 0.85$. These findings indicate that while FCC is the thermodynamically preferred bulk phase, HCP is the preferred phase at nucleation. The slope with which f_{FCC} approaches the end of the experiment is small, yet positive and amounts to $df_{\text{FCC}}/dt = 10^{-4} \text{ min}^{-1}$. Simulations have computed the rate of growth of FCC crystals at the expense of the HCP phase for hard spheres^[14b]; accordingly, this change should take only $\Delta t_{\text{sim}} = 1.8 \times 10^{-1} \text{ min}$ for a mixture of FCC and HCP crystal phases composed of 5.4 nm hard spheres to transition to a 1000 nm FCC crystal. However, experimentally we estimate $\Delta t_{\text{exp}} = (1 - 0.85)/(df_{\text{FCC}}/dt) \approx 1.5 \times 10^3 \text{ min}$ as the time for all the superstructures to show exclusive FCC ordering, a factor 8000 times larger than simulation predictions. This discrepancy may point to the impossibility of treating QDs as hard spheres at high volume fractions, and suggests that the role of the ligand may be crucial in the late-stage crystallization.

Further insight into the crystallization kinetics is obtained by calculating the lattice parameter, $a_{\text{FCC}}(t) = 2\pi\sqrt{3}/q_{111}(t)$, the surface-to-surface distance between nearest neighbors, $d_{\text{FCC}}(t) = [a_{\text{FCC}}(t)/\sqrt{2}] - \sigma_{\text{QD}}$, and the solid volume fraction $\phi_{\text{FCC}}(t) = (2\pi/3) \times [\sigma_{\text{QD}}/a_{\text{FCC}}(t)]^3 \times 100\%$, with a relative uncertainty, $\Delta\phi/\phi \leq 1\%$, estimated by the full-width at half-maximum Δq_{111} of the FCC(111) peak as shown in Figure 2e–g (see Supporting Information for details). During densification of the crystal, a_{FCC} decreases from 13.8 to 10.8 nm, corresponding to a decrease in d_{FCC} from 4.2 to 2.1 nm and an increase in ϕ_{FCC} from 14% to 30%. The smallest d_{FCC} values correspond to twice the effective ligand length, l , such that $\sigma_{\text{eff}} = \sigma_{\text{QD}} + 2l$ represents the effective hard-sphere size of the nanoparticle. An effective ligand length of $l = 1 \text{ nm}$ then results in an effective surface-to-surface distance $d_{\text{eff,FCC}} = 0$ and effective volume fraction reaching $\phi_{\text{eff,FCC}} = 73\%$ at the end of the experiment (Figure 2f,g), which is indeed in good agreement with the highest hard-sphere packing fraction of the FCC phase of 74%. This supports the idea that at high volume fractions, the oleate ligands bound to the QD surface behave as a $l = 1 \text{ nm}$ thick, hard shell stabilizing the QD cores.

In addition to average structural parameters, our X-ray measurements also provide insight into basic thermodynamic quantities and particle interactions. While the hard-sphere model is tempting and has been used to explain basic packing considerations,^[7c] nanoscale interactions mediated by ligands play an important role in the later stages of the dynamic assembly process. To obtain insight into these nanoscale interactions and their impact on crystallization, we increase the quench rate $d\phi/dt$ by raising the temperature from 40 to 80 °C, thus increasing the rate of evaporation of the emulsion droplets. The resulting evolution of the effective volume fraction shows ≈ 15 times faster rate indicated by the earlier sharp increase in volume fraction (Figure 3a). Remarkably, the characteristic shape is preserved for all quench rates, suggesting a common

mechanism of self-assembly and densification of the QD supercrystals. To show this most clearly, we rescale the time axis using $t^* = (t - t_x)/t_{70\%}$, where t_x corresponds to the inflection point in the volume fraction curves and $t_{70\%}$ is the characteristic time interval, in which the volume fraction reaches 70% (see Figure 3d); the rescaled curves show good agreement, with growth proceeding in a similar fashion independent of the quench rate. The crystal quality, however, is affected. Crystal domain sizes decrease overall with increasing quench rate, indicating deteriorating crystal quality as shown in Figure 3e. The crystal quality also depends on the choice of hydrophobic solvent, QD polydispersity, and surfactant concentration (Figures S9 and S10, Supporting Information).

Taking full advantage of the X-ray measurements, we use the structure factor for $q \rightarrow 0 \text{ nm}^{-1}$ to determine the compressibility, χ , and virial coefficient, B_2 , of the crystallizing particles. The osmotic compressibility is related to the low- q limit of the structure factor through $S(0) = b\chi$, where b is a positive constant.^[18] As the volume fraction increases, the compressibility decreases monotonically from $S(0) = 1$, typical for a colloidal gas, to $S(0) = 0$ at time t_c , when the material is no longer compressible (Figure 3b). The compressibility vanishes at $\phi \approx 55\%$, the hard-sphere melting transition, where the fluid–crystal coexistence ends and the material has completely converted into the crystal phase. This happens consistently for all quench rates. Furthermore, t_c coincides with the inflection point in the $\phi(t)$ curves, i.e., $t_c \approx t_x$, indicating that further increase of the volume fraction can only occur by compression of the crystal lattice.

We further determine the virial coefficient B_2 , a widely used measure of the thermodynamic state of attractive particles describing the balance of repulsive and attractive particle interactions.^[18c] Experimentally, the second virial coefficient B_2 is determined from the deviation $\Delta S(0)$ in the low- q limit (Figure 3f) according to $\Delta S(0) = S(0) - cB_2$,^[18b] where c is a positive constant. This virial coefficient is related to the effective pair potential $U(r)$ of the QDs via $B_2(T) = -2\pi \int_0^\infty (e^{-U(r)/k_B T} - 1)r^2 dr$, as shown in Figure 3c. In the case of $\Delta S(0) > 0$ ($B_2 < 0$), the dominant particle interactions are attractive, while for $\Delta S(0) < 0$ ($B_2 > 0$), the dominant interactions are repulsive. Initially, $\Delta S(0) = 0$ as expected for a colloidal gas of noninteracting particles. In contrast, at later times $t > t_c$, when the crystal lattice becomes compressed, $\Delta S(0)$ saturates at positive values, indicating attractive particle interactions. Interestingly, for the slowest quench, the particles become repulsive at intermediate times, possibly due to a slow spatial redistribution of sterically repulsive ligands bound to the QD.

We can understand the change from repulsive to attractive interactions from the compression-induced change in effective length of the stabilizing ligands. Using standard bond lengths and angles, an oleate ligand molecule can be approximated as a cylinder of length $l = 1.9 \text{ nm}$.^[19] However, at late stages, we measure $d_{\text{FCC}} \approx 2 \text{ nm} \equiv 2l$. Therefore, as the volume fraction increases during the evaporation of emulsion droplets, the effective length of the ligand chain must decrease. The effective ligand length can decrease either through ligand density redistribution around a QD, or interpenetration of ligand chains bound to neighboring particles.^[8] To elucidate these changes of particle interactions quantitatively,^[12a,20] we model the effective pair potential $U(d)$ as a superposition of a

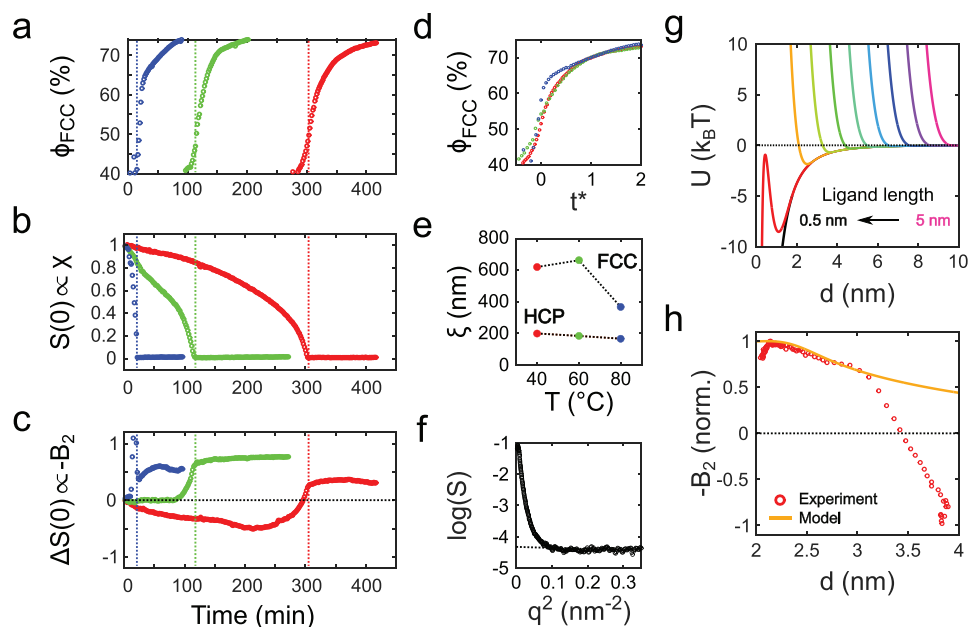


Figure 3. Evolution of experimental and modeled thermodynamic parameters. a–c) Time evolution of the effective volume fraction of the FCC phase (a), osmotic compressibility χ (b), and negative second virial coefficient $-B_2$ (c). Three quench rates are shown: fast quench (blue, 80 °C), medium quench (green, 60 °C), and slow quench (red, 40 °C). For the fast quench rate, cyclohexane has been used as apolar solvent rather than hexane because of the higher boiling point. For all quench rates, the compressibility vanishes when the QDs have fully crystallized. d) Effective volume fraction of the FCC phase as a function of rescaled time t^* indicating good overlap for the three quench rates. e) Final resulting average crystalline domain size for the three quench rates. f) Schematic illustrating extraction of $S(0)$ and $\Delta S(0)$ from $S(q)$ data. To determine $S(0)$, $\log(S)$ is plotted as a function of q^2 and linearly extrapolated to $q^2 = 0$ using the linear fitting function $h(q^2)$ (dotted line). To determine $\Delta S(0)$, the third-degree polynomial fitting of $\log(S) - h(q^2)$ is extrapolated to $q^2 = 0$.^[18b] g) Modeling of the pair potential $U(d)$ of the 5.4 nm spherical QDs subjected to van der Waals attraction and steric repulsion for various ligand length, l , decreasing from 5 to 0.5 nm in steps of 0.5 nm from right to left. h) Comparison of measured and modeled second virial coefficient as a function of surface-to-surface distance between QDs.

repulsive steric component U_{steric} ,^[21] and a short-ranged attractive van der Waals component, U_{vdw} ,^[22] (see Supporting Information for details). The resulting potential, $U = U_{\text{steric}} + U_{\text{vdw}}$, as a function of ligand length l for 5.4 nm spherical QDs and a ligand surface coverage of 3 nm^{-2} ,^[23] shows a shallow attractive secondary minimum arising when the ligand length l becomes smaller than 2 nm (Figure 3g and Figure S6, Supporting Information). This secondary minimum deepens as the ligand length decreases, until the steric repulsion becomes insufficient and the potential is dominated by the primary van der Waals minimum. This is indeed in general agreement with the excellent colloidal stability of QDs stabilized with long oleate ligands, and their limited stability when stabilized with shorter ligands. The measured surface-to-surface distance d_{FCC} decreases until $d_{\text{FCC}} = 2 \text{ nm}$ at late times, implying $l = 1 \text{ nm}$. This causes a gentle but progressive destabilization of QDs subjected to increasingly attractive interactions that are initially small enough to allow an equilibrium crystalline phase to form, later leading to permanent assembly.^[24] A quantitative comparison of predicted and measured second virial coefficient B_2 for the slow quench (Figure 3h and Figure S6, Supporting Information) shows good agreement for short surface-to-surface distances, while deviating at larger particle separations, likely due to additional repulsive components such as electrostatic interactions that are not included in the model. This agreement at short distances indeed supports the idea that when compressed, the QDs exhibit attractive van der Waals forces

that eventually arrest them into stable supercrystals. We finally investigate the generality of this approach by using lead sulfide, PbS, QDs passivated with the same oleate ligands (Figure S8, Supporting Information).^[25] We find great similarity with the CdSe dots used here, indicating that these results are general, and not limited to a particular QD core material.

SAXS proves to be an extremely sensitive technique to monitor the crystallization kinetics and energetics of colloidal QDs during the emulsion-templated assembly. The transitioning from a colloidal gaseous to a solid phase at an effective volume fraction of 55% is compatible with an effective hard-sphere model, including the volume occupied by the ligands. Grown supercrystals at the end of the assembly exhibit close to 74% effective volume fraction and 85% FCC packing, expected to ripen to 100% in roughly 24 hours, while late stages are governed by increasing van der Waals attraction. This novel assembly approach yields spherical and crystalline superstructures approaching single-crystal quality and sizes up to $1 \mu\text{m}$ in a matter of minutes. The rapid and facile production shown here is therefore encouraging for the large-scale realization of bottom-up QD-based artificial solids. Additionally, through droplet microfluidics, the emulsion polydispersity can be narrowed to such a degree that the resulting supercrystals may be packed into hypercrystals, ordered on three distinct length scales. The hypercrystalline order will lie in the range of the visible spectrum, enabling interesting photonic applications based on all-QD devices. Furthermore, the prospect

of exchanging insulating oleates for conductive ligands while preserving the long-range order within supercrystals will facilitate coherent electronic transport over large distances. We expect this combination of order with transport to substantially improve QD devices such as solar cells and photodetectors.

Supporting Information

Supporting Information is available from the Wiley Online Library or from the author.

Acknowledgements

The authors thank K. Dohnalova, G. Grimaldi, T. Gregorkiewicz, and J. Sprakel for helpful discussions, and R.W. Crisp for a thorough reading of the manuscript. Beamtime at BM26B "DUBBEL" beamline, ESRF was supported through NWO funding (experiment no. 26-02-841). The authors also thank D.H. Merino and A. Capretti for assistance with X-ray data collection. T.E.K. and P.S. acknowledge support by VENI and VICI, respectively, personal grants from the Nederlandse Organisatie voor Wetenschappelijk Onderzoek (NWO).

Conflict of Interest

The authors declare no conflict of interest.

Keywords

nanocrystals, nanoparticle assembly, quantum dots, SAXS, supercrystals

Received: May 30, 2018

Revised: July 11, 2018

Published online: August 21, 2018

- [1] a) T.-H. Kim, K.-S. Cho, E. K. Lee, S. J. Lee, J. Chae, J. W. Kim, D. H. Kim, J.-Y. Kwon, G. Amaratunga, S. Y. Lee, B. L. Choi, Y. Kuk, J. M. Kim, K. Kim, *Nat. Photonics* **2011**, *5*, 176; b) Y. Yang, Y. Zheng, W. Cao, A. Titov, J. Hyvonen, J. R. Manders, J. Xue, P. H. Holloway, L. Qian, *Nat. Photonics* **2015**, *9*, 259.
- [2] a) I. Nikitskiy, S. Goossens, D. Kufer, T. Lasanta, G. Navickaite, F. H. L. Koppens, G. Konstantatos, *Nat. Commun.* **2016**, *7*, 11954; b) R. Saran, R. J. Curry, *Nat. Photonics* **2016**, *10*, 81.
- [3] A. Swarnkar, A. R. Marshall, E. M. Sanehira, B. D. Chernomordik, D. T. Moore, J. A. Christians, T. Chakrabarti, J. M. Luther, *Science* **2016**, *354*, 92.
- [4] J. Lim, Y.-S. Park, V. I. Klimov, *Nat. Mater.* **2017**, *17*, 42.
- [5] V. I. Klimov, A. A. Mikhailovsky, S. Xu, A. Malko, J. A. Hollingsworth, C. A. Leatherdale, H.-J. Eisler, M. G. Bawendi, *Science* **2000**, *290*, 314.
- [6] H. Scher, R. Zallen, *J. Chem. Phys.* **1970**, *53*, 3759.
- [7] a) X. Ye, J. Chen, M. E. Irrgang, M. Engel, A. Dong, S. C. Glotzer, C. B. Murray, *Nat. Mater.* **2017**, *16*, 214; b) E. V. Shevchenko, D. V. Talapin, N. A. Kotov, S. O'Brien, C. B. Murray, *Nature* **2006**, *439*, 55; c) W. H. Evers, B. D. Nijs, L. Fillion, S. Castillo, M. Dijkstra, D. Vanmaekelbergh, *Nano Lett.* **2010**, *10*, 4235.
- [8] a) M. A. Boles, D. V. Talapin, *J. Am. Chem. Soc.* **2015**, *137*, 4494; b) D. Vanmaekelbergh, *Nano Today* **2011**, *6*, 419.
- [9] a) F. Montanarella, T. Altantzis, D. Zanaga, F. T. Rabouw, S. Bals, P. Baesjou, D. Vanmaekelbergh, A. van Blaaderen, *ACS Nano* **2017**, *11*, 9136; b) D. Vanmaekelbergh, L. K. van Vugt, H. E. Bakker, F. T. Rabouw, B. de Nijs, R. J. A. van Dijk-Moes, M. A. van Huis, P. J. Baesjou, A. van Blaaderen, *ACS Nano* **2015**, *9*, 3942; c) B. de Nijs, S. Dussi, F. Smalenburg, J. D. Meeldijk, D. J. Groenendijk, L. Fillion, A. Imhof, A. van Blaaderen, M. Dijkstra, *Nat. Mater.* **2014**, *14*, 56; d) J. Lacava, P. Born, T. Kraus, *Nano Lett.* **2012**, *12*, 3279; e) T. Kister, M. Mravlak, T. Schilling, T. Kraus, *Nanoscale* **2016**, *8*, 13377.
- [10] a) O. L. Lazarenkova, A. A. Balandin, *J. Appl. Phys.* **2001**, *89*, 5509; b) J.-H. Choi, A. T. Fafarman, S. J. Oh, D.-K. Ko, D. K. Kim, B. T. Diroll, S. Muramoto, J. G. Gillen, C. B. Murray, C. R. Kagan, *Nano Lett.* **2012**, *12*, 2631.
- [11] B. D. Chernomordik, A. R. Marshall, G. F. Pach, J. M. Luther, M. C. Beard, *Chem. Mater.* **2017**, *29*, 189.
- [12] a) K. J. M. Bishop, C. E. Wilmer, S. Soh, B. A. Grzybowski, *Small* **2009**, *5*, 1600; b) M. A. Boles, D. Ling, T. Hyeon, D. V. Talapin, *Nat. Mater.* **2016**, *15*, 141.
- [13] V. N. Manoharan, M. T. Elsesser, D. J. Pine, *Science* **2003**, *301*, 483.
- [14] a) P. G. Bolhuis, D. Frenkel, S.-C. Mau, D. A. Huse, *Nature* **1997**, *388*, 235; b) S. Pronk, D. Frenkel, *J. Chem. Phys.* **1999**, *110*, 4589; c) S.-C. Mau, D. A. Huse, *Phys. Rev. E* **1999**, *59*, 4396.
- [15] J. J. Geuchies, C. van Overbeek, W. H. Evers, B. Goris, A. de Backer, A. P. Gantapara, F. T. Rabouw, J. Hilhorst, J. L. Peters, O. Konovalov, A. V. Petukhov, M. Dijkstra, L. D. Siebbeles, S. van Aert, S. Bals, D. Vanmaekelbergh, *Nat. Mater.* **2016**, *15*, 1248.
- [16] M. C. Weidman, Q. Nguyen, D.-M. Smilgies, W. A. Tisdale, *Chem. Mater.* **2018**, *30*, 807.
- [17] C. B. Murray, C. R. Kagan, M. G. Bawendi, *Science* **1995**, *270*, 1335.
- [18] a) A. Guinier, *X-Ray Diffraction: In Crystals, Imperfect Crystals, and Amorphous Bodies*, W. H. Freeman & Company, San Francisco, CA, USA **1963**; b) H. Matoussi, A. W. Cumming, C. B. Murray, M. G. Bawendi, R. Ober, *Phys. Rev. B* **1998**, *58*, 7850; c) D. E. Stogryn, J. O. Hirschfelder, *J. Chem. Phys.* **1959**, *31*, 1531.
- [19] F. D. Gunstone, J. L. Harwood, A. J. Dijkstra, *The Lipid Handbook with CD-ROM*, CRC Press, Boca Raton, FL, USA **2007**.
- [20] L. Wu, J. J. Willis, I. S. McKay, B. T. Diroll, J. Qin, M. Cargnello, C. J. Tassone, *Nature* **2017**, *548*, 197.
- [21] J. U. Kim, M. W. Matsen, *Macromolecules* **2008**, *41*, 4435.
- [22] J. N. Israelachvili, *Intermolecular and Surface Forces*, Academic Press, San Diego, CA, USA **2011**.
- [23] N. C. Anderson, M. P. Hendricks, J. J. Choi, J. S. Owen, *J. Am. Chem. Soc.* **2013**, *135*, 18536.
- [24] V. J. Anderson, H. N. W. Lekkerkerker, *Nature* **2002**, *416*, 811.
- [25] M. C. Weidman, M. E. Beck, R. S. Hoffman, F. Prins, W. A. Tisdale, *ACS Nano* **2014**, *8*, 6363.